15 May 2020

Utility Of Vertically Integrated Liquid Water Content For Radar-Rainfall Estimation: Quality Control And Precipitation Type Classification

Bong Chul Seo
Missouri University of Science and Technology, bongchul.seo@mst.edu

Witold F. Krajewski

Youcun Qi

Recommended Citation

B. C. Seo et al., "Utility Of Vertically Integrated Liquid Water Content For Radar-Rainfall Estimation: Quality Control And Precipitation Type Classification," *Atmospheric Research*, vol. 236, article no. 104800, Elsevier, May 2020.
The definitive version is available at https://doi.org/10.1016/j.atmosres.2019.104800

Atmospheric Research 236 (2020) 104800

Contents lists available at ScienceDirect

Atmospheric Research

journal homepage: www.elsevier.com/locate/atmosres

Utility of Vertically Integrated Liquid Water Content for Radar-Rainfall Estimation: Quality Control and Precipitation Type Classification

Bong-Chul Seo[a,*], Witold F. Krajewski[a], Youcun Qi[b]

[a] IIHR—Hydroscience & Engineering, The University of Iowa, Iowa City, IA 52242, USA
[b] Institute of Geographic Sciences and Natural Resources Research, Chinese Academy of Sciences, Beijing, China

ARTICLE INFO

Keywords:
VIL
Weather radar
Precipitation
Classification
Wind farms

ABSTRACT

This study proposes a new estimation method for vertically integrated liquid water content (VIL) using radar reflectivity volume data and temperature sounding retrieved from the numerical weather model analysis. This method addresses uncertainty factors in conventional VIL estimation associated with the effects from the bright band (BB) and radar beam geometry near the radar site. The new VIL is then used for precipitation classification (convective/stratiform) and wind turbine clutter detection in the hope that the estimated VIL indicating vertical activities or development of precipitation systems will account for the two independent subjects together, in opposite ways. The non-precipitation radar echoes returned from wind turbines do not likely generate significant degree of VIL, compared to the one estimated from actual convective cells, which contain comparable reflectivity strength. We tested the proposed VIL estimation, precipitation classification, and wind turbine clutter detection methods using various Iowa cases and illustrated their successful application. We also performed a quantitative evaluation of precipitation classification using ground reference data from a dense rain gauge network over the Turkey River basin in Iowa. The evaluation results show improved performance for most non-convective event cases estimated by the stratiform estimator ($Z = 200R^{1.6}$) because we applied the convective estimator ($Z = 300R^{1.4}$) to all event cases without classification. In addition, we demonstrated the potential of the new classification to mitigate significant BB effects in quantitative precipitation estimation using a correction method based on the vertical profile of reflectivity.

1. Introduction

Vertically integrated liquid water content (VIL) is an estimate of liquid (precipitation) mass within a column of air/clouds. It is generally obtained by the vertical integration of radar reflectivity observations (Greene and Clark 1972). Before enhanced capabilities (e.g., dual-polarization) are available from radar observations, operational forecasters applied this quantity to severe weather warnings, particularly for hail detection and thunderstorm tracking (e.g., Johnson et al. 1998; Witt et al. 1998; Skripniková and Řezáčová 2014), as well as to the validation of cloud models (e.g., Löhnert et al. 2004). Because both hail and thunderstorms imply the presence of convection, many studies (e.g., Matrosov 2009; Zhang and Qi 2010; Qi et al. 2013) have introduced VIL into precipitation estimation procedures to discriminate precipitation types (convective or stratiform), which are characterized by different raindrop size distributions (DSD). The variability of DSD is one of the substantial error sources in quantitative precipitation estimation (QPE), and different types of DSD often require different estimators to improve QPE accuracy (e.g., Chapon et al. 2008). Other than the VIL application, many other classification approaches exist; these include the use of neural networks, observed rainfall intensity at the surface, and DSD parameters (e.g., Anagnostou 2004; Llasat et al. 2007; Caracciolo et al. 2008). The classification also serves as a required first step for the application of the vertical profile of reflectivity (VPR) correction (e.g., Creutin et al. 1997; Zhang and Qi 2010) to mitigate the bright band (BB) effects in QPE.

Radar observations contain a variety of error sources (e.g., Villarini and Krajewski 2010), and some of which become major uncertainty factors in the VIL estimation (e.g., French et al. 1995; Boudevillain and Andrieu 2003). Among these, BB often causes significant VIL overestimation, which may lead to the misclassification of stratiform to convective precipitation. The presence of BB is typically an indicator of stratiform precipitation (e.g., Stewart et al. 1984). Radar beam geometry provides another practical challenge when estimating VIL for the region near the radar site. VIL is usually underestimated because of the radar beam's poor vertical coverage near the radar site (e.g., the so-

* Corresponding author at: Bong-Chul Seo, IIHR—Hydroscience & Engineering, The University of Iowa, Iowa City, IA, 52242, USA.
E-mail address: bongchul-seo@uiowa.edu (B.-C. Seo).

https://doi.org/10.1016/j.atmosres.2019.104800
Received 15 May 2019; Received in revised form 5 November 2019; Accepted 2 December 2019
Available online 03 December 2019

called “cone of silence”), which makes it harder to detect a convective system in that area. As such, some classification studies (e.g., Qi et al. 2013) switch to another decision factor (e.g., VIL to reflectivity) for that range (e.g., < 25 km). On the other hand, some non-precipitation radar echoes (e.g., those returned from wind turbines) might yield some degree of VIL associated with the vertical beam width at the turbine locations. Despite enhanced capabilities (e.g., dual-polarization) of modern radars, the elimination of these echoes has been quite challenging because the turbines are generally clustered to augment the efficiency of energy generation (e.g., Kusiak and Song 2010), and their interactions with radar beam often show features similar to intense precipitation (e.g., Seo et al. 2015b; Zhang et al. 2016). However, the turbine clutter does not seem to generate considerable degree of VIL compared to actual convective cells that have reflectivity strength similar to the clutter echoes. Therefore, the primary objectives of this study are: (1) to propose a new VIL estimation method that can reduce the effects from the aforementioned uncertainty factors (e.g., BB and radar beam geometry); and (2) to examine the two independent issues of precipitation classification and wind turbine clutter detection together, based on the improved VIL estimation. This approach is feasible because both issues are likely represented in opposite ways by the vertical activities or development of precipitation systems. Our basic classification/detection strategy is to use VIL consistently over the entire radar range without switching to another decision factor. We note that all the components proposed in this study were developed as part of the Iowa Flood Center (IFC) operational QPE algorithm (e.g., Krajewski et al. 2017).

The paper is structured as follows. In Section 2, we outline this study's methodology for the VIL estimation, precipitation type and wind turbine clutter classification, and evaluation of the proposed method. Section 3 provides detailed algorithmic procedures for the elements described in Section 2, including required parameters and their qualitative test results using a variety of Iowa cases. Section 4 evaluates the proposed precipitation classification method using ground reference data and demonstrates its potential for the VPR correction. In Section 5, we summarize and discuss the main findings and relevant future work.

2. Methodology

In this section, we define VIL and provide its estimation procedures using radar observations and temperature sounding retrieved from the analysis of a numerical weather prediction model. The temperature sounding data are used to mitigate VIL overestimation affected by the melting layer effect (e.g., BB). We briefly describe schemes for precipitation type (convective/stratiform) classification and wind turbine clutter detection based on the estimated VIL. We then specify weather radar and reference data (e.g., rain gauge) sets used for the algorithm development and testing and outline the evaluation of the proposed method in this study.

2.1. VIL

Liquid water content indicates the degree of condensation and precipitation development and can be determined using radar measurements with an assumption about the DSD. Using an exponential DSD (Marshall and Palmer 1948) and radar reflectivity (Z, mm^6/m^3) presented in Eqs. (1) and (2), liquid water content (LW, kg/m^3) is derived in Eq. (3):

$$n(D) = N_0 \exp(-\lambda D) \tag{1}$$

$$Z = \int_0^x n(D) D^6 dD \tag{2}$$

$$\mathrm{LW} = \frac{\rho_w \pi}{6} \int_0^x n(D) D^3 dD = 3.44 \times 10^{-6} Z^{4/7} \tag{3}$$

where D, N_0, and λ denote drop diameter (mm), concentration (m^{-4}), and size parameters (m^{-1}), respectively. x is the maximum drop diameter, and ρ_w is the density of water (kg/m^3). Further detailed derivation of Eq. (3) is provided in Greene and Clark (1972). For a given radar gate (r) location, VIL (kg/m^2) is estimated by the vertical integration of LW, calculated using radar reflectivity measurements at multiple tilt angles:

$$\mathrm{VIL} = \sum_{i=1}^{n} \mathrm{VIL}_i$$

$$\mathrm{VIL}_i = \int_{h_{i,bottom}(r)}^{h_{i,top}(r)} \mathrm{LW}_{i,r}\, dh = 3.44 \times 10^{-6} \int_{h_{i,bottom}(r)}^{h_{i,top}(r)} Z_{i,r}^{4/7}\, dh \tag{4}$$

where n is the number of radar tilts, and $h_i(r)$ denotes the radar beam altitude of ith tilt at a given gate location. While the subscripts, *top* and *bottom* in Eq. (4) indicate the highest and lowest radar beam altitudes related to the vertical beam width at a given location, their practical calculation for the VIL estimation is provided in many studies (e.g., Zhang and Qi 2010; Qi et al. 2013).

The VIL estimation using radar reflectivity measurements in Eq. (4) has two weaknesses: (1) VIL underestimation near the radar site due to the poor vertical coverage of radar volume structure; and (2) VIL overestimation in the regions affected by the BB (e.g., significant reflectivity enhancement). For a range near the radar site, the conventional VIL approach integrates reflectivity values at each tilt over the respective vertical intervals/distances that are relatively short. Furthermore, most tilt elevations at this range is generally much lower than the altitudes where convective systems are active, and this leads to VIL underestimation at the range. We attempt to mitigate this underestimation by specifying a constant altitude range (e.g., 20 km) within a radar domain for the VIL estimation. The use of an altitude limit (20 km) is based on the updraft measurements of convection clouds studied in the prior research (e.g., Auer and Sand 1966). For those radar ranges where the altitude of the highest tilt is below 20 km, we uniformly expand observed reflectivity at the highest tilt up to 20 km after checking the vertical continuity of reflectivity. The continuity check inspects sudden enhancement of reflectivity at the highest tilt compared to that at the second highest tilt to mitigate the BB effect at the highest tilt. This extrapolation may exaggerate VIL quantities for some convective systems (observed at the highest tilt) that pass the vicinity of the radar site. Therefore, we use the estimated VIL for the classification of precipitation types (convective/stratiform) only and do not directly use it for rain rate estimation. The melting layer (e.g., BB effect) is another important factor that can contaminate the VIL estimation because of strong reflectivity enhancement—for example at the highest tilt near the radar site. To avoid the effect from this contamination at all radar ranges, we adjust observed reflectivity values (only for the VIL estimation) that are likely affected by the BB using the temperature sounding and local VPR structure. We retrieve the temperature sounding data from the Rapid Refresh (Benjamin et al. 2016) model analysis. The Rapid Refresh is a continental-scale, hourly-updated assimilation and model forecast system based on a 13 km resolution horizontal grid. We describe the algorithm details of VIL estimation and provide some example cases to demonstrate the effectiveness of the proposed scheme in the next section (Section 3).

2.2. Classification

In this study, we use two types of classification based on the estimated VIL in Eq. (4): (1) the separation of precipitation types into convective/stratiform regions; and (2) the detection of wind turbine clutter. The precipitation classification employs a VIL threshold of 6.5 kg/m^2 to define convective cores within precipitation regions. This threshold applied to the entire network of the U.S. Weather Surveillance Radar-1988 Doppler (WSR-88D) radars demonstrated good performance in the studies of Zhang and Qi (2010) and Qi et al. (2013). We then use a seeded region-growing method (Adams and Bischof 1994) to

expand the convective areas centered on the detected cores by aggregating pixels based on the inspection of surrounding pixel values. This procedure is required to define a boundary of convective rain and to mitigate misclassifications of some convective cells into stratiform rain caused by the use of a fixed VIL threshold (Qi et al. 2013). As an aggregating factor for this method, we use a VIL average of surrounding pixels, while Qi et al. (2013) applied an average of those pixels' reflectivity (e.g., a threshold of 35 dBZ). We note that the use of reflectivity for region-growing might be vulnerable to the effect of the melting layer within which radar reflectivity is significantly enhanced (e.g., Austin and Bemis 1950; Zhang and Qi 2010). We decided to use the threshold of VIL average (4.0 kg/m^2) based on the results of the qualitative case studies and quantitative evaluation using a few different VIL average values, as presented in section 3.2.

In the proposed approach, we put forward the following basic idea to distinguish wind turbine effects: the estimated VILs for the clutter locations should be relatively low despite the strong reflectivity values observed in the locations. This is because radar observations at the lowest tilts are typically contaminated by the interactions between radar beam and wind turbine wakes (e.g., Seo et al. 2015b). To detect likely returns from wind turbine effects, the proposed algorithm uses adaptive VIL thresholds conditioning on reflectivity values (e.g., VIL $<$ 2.0 kg/m^2 for $Z >$ 50 dBZ; VIL $<$ 1.0 kg/m^2 for $Z >$ 25 dBZ). We determined these threshold values based on the comparison of VIL distributions between expert-selected obvious rain and wind turbine cases. For the detected clutter locations, we perform a vertical continuity check once more and then expand the clutter regions because wind turbines are typically clustered to maximize wind energy generation (e.g., Kusiak and Song 2010). We use the reflectivity average of surrounding pixels (e.g., 15 and 40 dBZ) as an aggregating parameter in the growing algorithm. The use of these threshold values is a subjective decision based on our experience. While the clutter identification for no rain area is relatively easier, it is even harder to detect clutter embedded in rain echoes. Therefore, a higher threshold value (e.g., 40 dBZ) is required to preserve actual rain echoes for rain areas. The use of reflectivity for this process does not seem to be affected by the melting layer.

2.3. Testing and evaluation

Because the proposed method is motivated by the needs of the IFC QPE algorithms, we use data from the WSR-88D radars in the Iowa domain for development and evaluation of the algorithm in this study. The WSR-88D system description, its data collection, and enhanced polarimetric capability are provided in Crum and Alberty (1993), Crum et al. (1993), and Ryzhkov et al. (2005), respectively. Fig. 1 shows the locations of the involved radars covering Iowa, and data from some of these radars (e.g., KARX, KDVN, KDMX, and KOAX) are used as illustrated in Sections 3 and 4. The locations of clustered wind turbines (e.g., wind farm) are also presented in Fig. 1. Iowa is a relatively flat area with some rolling hills, and there is no significant terrain and orographic effect in the study domain. We provide both qualitative and quantitative analyses to demonstrate and verify the utility of the proposed VIL estimation and classification methods. In particular, we assess the usefulness of our precipitation classification by evaluating improvement in QPE. This requires a high-quality, high-density ground reference (e.g., rain gauge) network that can capture the dynamic aspects of precipitation movements, evolution, and spatial coverage change of each precipitation type. Therefore, we selected a network containing 20 rain gauges within the Turkey River basin in Iowa (see Fig. 1) and collected hourly data for a period of 1 May–15 June 2013, during which time we hosted a NASA field campaign known as Iowa Flood Studies or IFloodS (e.g., Quintero et al., 2016; Seo et al. 2018). We note that the QPE product employed in the evaluation was generated using the data from the KARX radar that is the closest one to the rain gauge network. The distances between the KARX radar and the rain gauges are 80–120 km, and an average inter-gauge distance between nearest rain gauges within the network is 13.2 km. The network consisted of dual tipping-bucket gauges at all 20 sites; their maintenance and quality controls are documented in Seo et al. (2015a). For a quantitative measure, we use several statistical metrics of multiplicative bias (B), correlation (r), mean absolute error (MAE), and root mean square error (RMSE). Because these metrics have been widely used in several meteorological and hydrologic studies (e.g., Seo et al. 1999; Li et al. 2017), we do not provide their detailed formulas here. We also note that the evaluation of wind turbine clutter detection is limited to qualitative assessment only because rain gauges deployed near the wind turbines are quite rare.

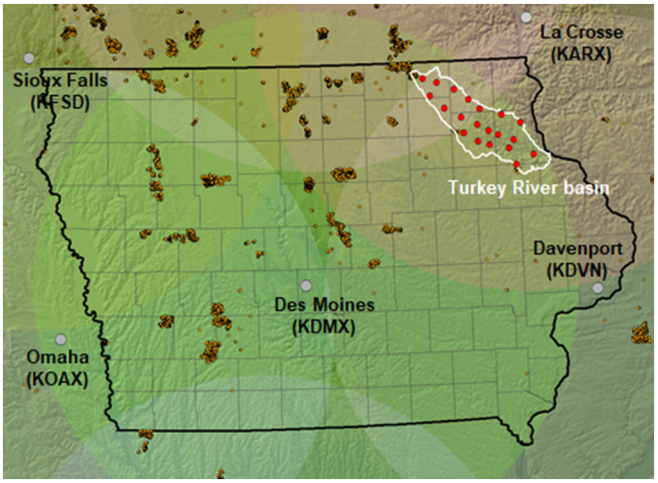

Fig. 1. The domain of this study and WSR-88D radar locations covering Iowa. The black solid line and the circular zones indicate the Iowa border and each individual radar domain (230 km from the radar), respectively. The red dots represent 20 rain gauge locations within the Turkey River basin (white solid line) in Iowa. The clustered orange dots indicate wind farm locations as of 2015. (For interpretation of the references to colour in this figure legend, the reader is referred to the web version of this article.)

3. Algorithm development and testing

3.1. VIL estimation

VIL estimation begins with construction of a two-dimensional (polar-based) reference map of reflectivity that contains reflectivity observations below the melting layer. This reference map supports inspection of the vertical variability of reflectivity at each grid location. We use the temperature sounding data to define an altitude range associated with the melting layer. Figs. 2 and 3 illustrate two example BB cases that show considerable reflectivity enhancement (e.g., about 3–5 dB) within the melting layer. The VPRs and temperature sounding presented in Fig. 3 were sampled from and averaged over a range of 30–80 km from each radar. Some tests (not provided) on several temperature profiles retrieved from the Rapid Refresh model grids within the sampling zone confirmed that they have insignificant variability within the sampling zone, and its effect on the VPR variability should be considered negligible. Therefore, temperature profiles retrieved from coarse horizontal resolution data such as North American Regional Reanalysis (Mesinger et al. 2006) could be used for other geographic regions where high resolution data are barely available.

Based on the two cases in Figs. 2 and 3, we identify a temperature zone above 5 °C as the region below the melting layer and include the lowest tilt (reflectivity) data observed from this region in the reference map. For regions where the lowest tilt intersects with the melting layer (e.g., between 5 and − 5 °C), we select the tilt data closest to the temperature of about −5 °C as reference values. Once the reference

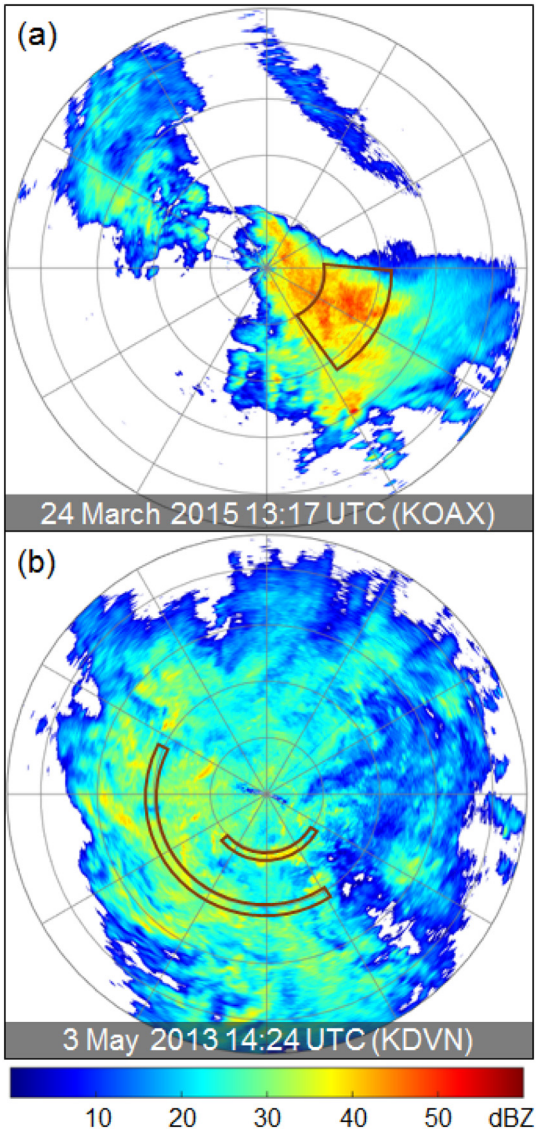

Fig. 2. Base scan (approximately 0.5° elevation angle) reflectivity maps for two example BB cases observed from the KOAX and KDVN radars. The red circular bands in the maps indicate the regions affected by the BB effect. The maximum range shown in the map is 230 km, and the circular lines centered on the radars demarcate every 50 km distance from the radars. (For interpretation of the references to colour in this figure legend, the reader is referred to the web version of this article.)

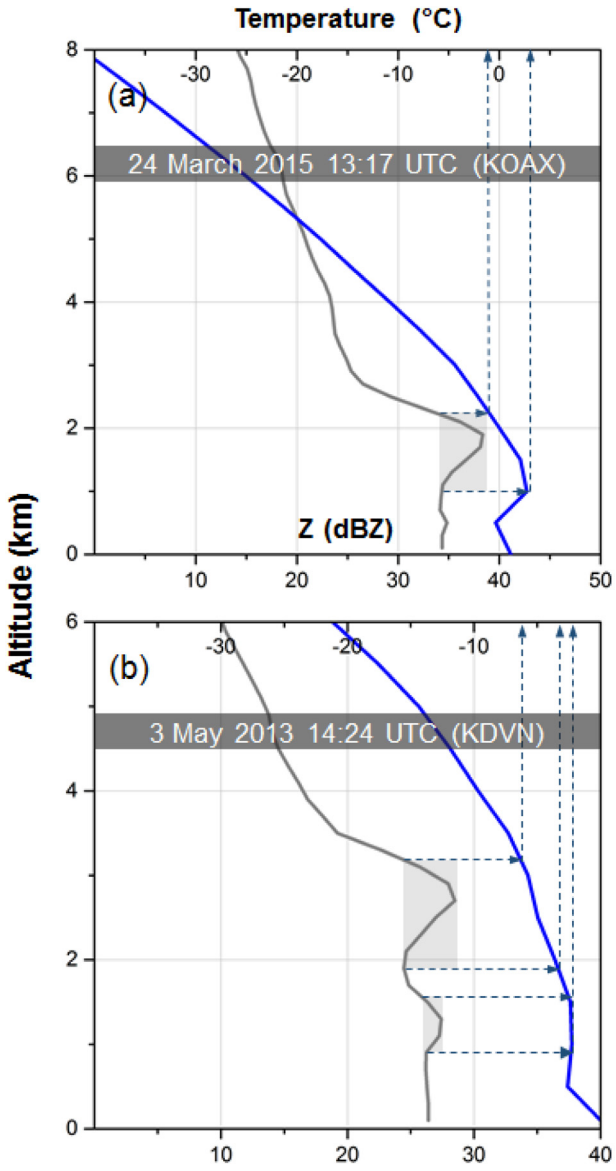

Fig. 3. Estimated VPRs (gray solid lines) and retrieved temperature sounding (blue solid lines) for the cases presented in Fig. 2. The gray-colored areas and dashed arrows indicate the temperature ranges associated with the BB effect (e.g., reflecivity enhancement). (For interpretation of the references to colour in this figure legend, the reader is referred to the web version of this article.)

map is complete, we then examine VPRs at all grid locations and replace reflectivity values that show strong enhancement within the melting layer with the one in the reference map. The VIL estimation procedure described in Eq. (4) integrates this adjusted reflectivity field vertically up to 20 km depending on the WSR-88D's volume coverage pattern (e.g., Brown et al. 2005) and creates a two-dimensional VIL map as illustrated in Fig. 4. Fig. 4 compares the proposed VIL estimation with the conventional estimation with/without a 20 km altitude limitation and demonstrates that the proposed estimation successfully reduces the BB effect for the two cases shown in Figs. 2 and 3. The clear BB effect appears in Fig. 4, and the mitigation of this effect in the VIL estimation leads to an improved precipitation classification because a system with the melting layer should be identified as stratiform precipitation.

3.2. Classification of precipitation types

As described in Section 2.2, classification involves two steps: (1) identification of convective cores using a VIL threshold; and (2) expansion of areas centered on the cores using the VIL structure of neighboring pixels. After these two steps, the remaining rain pixels are defined as stratiform regions. While the first step is quite simple (e.g., binary thresholding), the subsequent one requires an aggregating factor to grow the convective regions. For the aggregating factor, we do not use reflectivity to inspect neighboring pixels. The use of reflectivity is likely inappropriate because reflectivity enhanced by the BB effect often results in overgrowing, which entails another decision on which tilt data should be selected for the neighboring pixel values. Therefore, we use the estimated VIL to simplify the proposed classification procedures (as it is employed in the first step) and define the region-growing parameter as an average of surrounding VIL values.

We tested a variety of cases (e.g., over 50 cases) observed from multiple radars to decide on the parameter values and inspected the

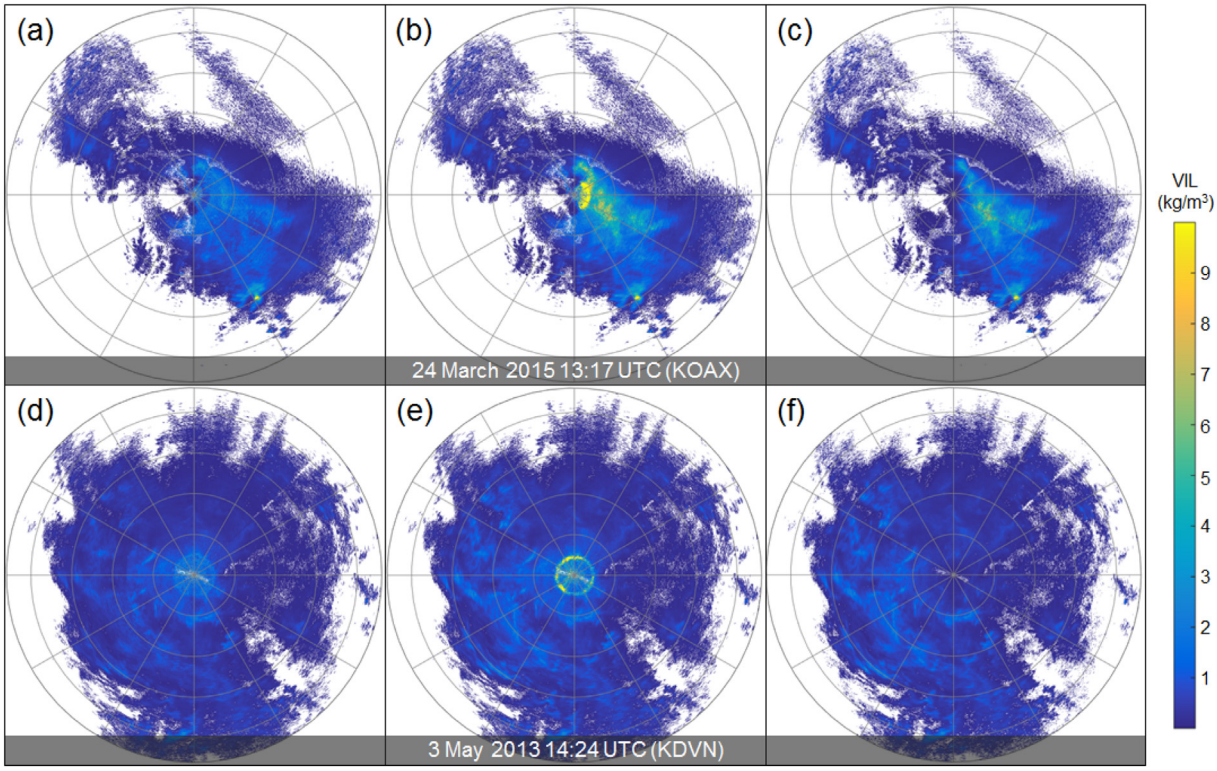

Fig. 4. Maps of estimated VIL for the BB cases presented in Fig. 2. (a) and (d): the proposed VIL estimation in this study; (b) and (e): the conventional method with a 20 km altitude limitation; and (c) and (f): conventional estimation. The annular patterns near the radar site shown in (b) and (e) were because of reflectivity enhancement at the highest elevation angle and its extrpolation up to 20 km. (a) and (d) demonstrate that the proposed VIL estimation mitigates clear BB effects observed in (b), (c), and (e).

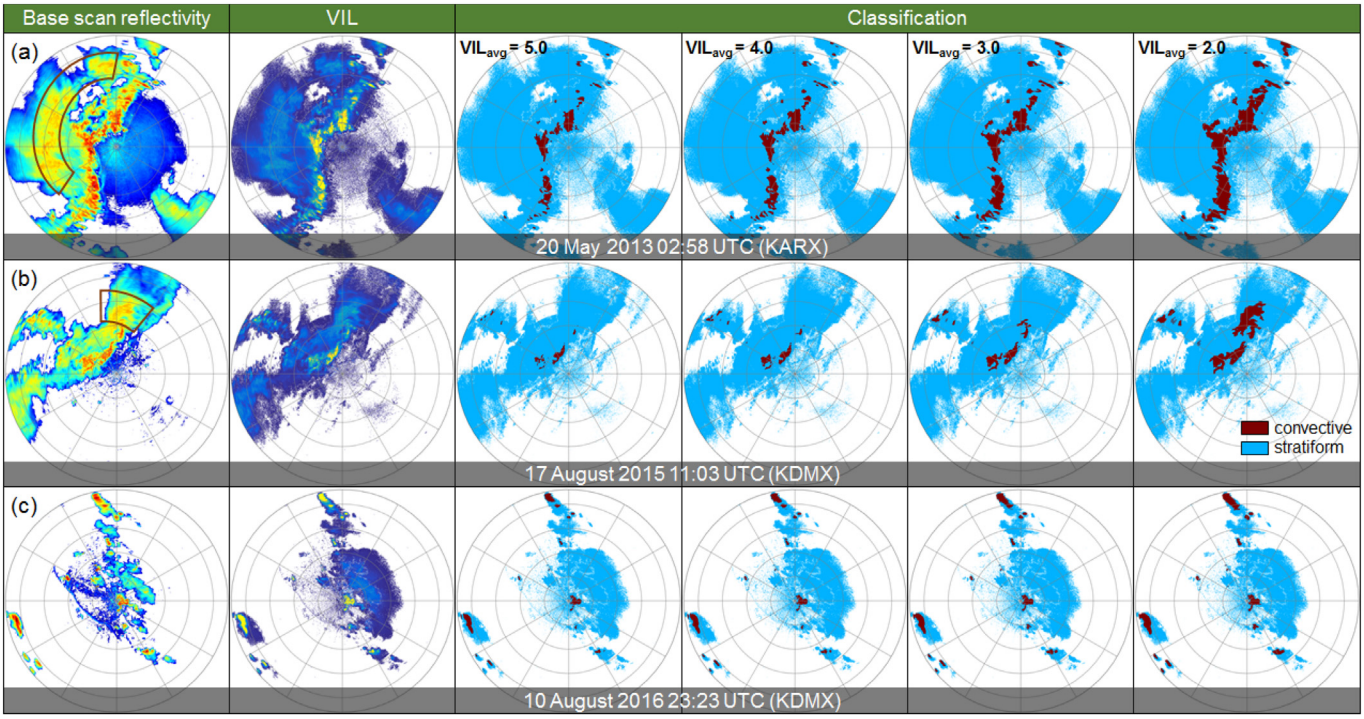

Fig. 5. Maps of base scan reflectivity, VIL, and precipitation classification (with different region-growing parameters) for three example cases observed by the KARX and KDMX radars. The red circular bands in the reflectivity maps of (a) and (b) indicate the regions affected by the BB effect. Each colour scale used for the reflectivity and VIL maps is identical to the ones in Figs. 2 and 4, respectively. (For interpretation of the references to colour in this figure legend, the reader is referred to the web version of this article.)

maps of base scan reflectivity, estimated VIL, and precipitation classification (representative cases are shown in Fig. 5). Overall, our VIL estimation demonstrates effective control of the effects from the BBs observed in Fig. 5(a) and (b). The BB effects are indicated by circular bands in Fig. 5. The classification maps in Fig. 5 show that the convective regions become gradually larger as the parameter (VIL average of neighboring pixels, VIL_{avg}) value decreases. However, relatively small parameter value often yields erroneous expansion to the regions affected by the BB, as shown in the map ($VIL_{avg} = 2.0$) of Fig. 5(b). A prominent aspect of the proposed approach is that convective storms in the vicinity of the radar site can be successfully captured, as presented in Fig. 5(c). This was challenging because of the deficient vertical coverage at close radar ranges. To determine the region-growing parameter, we performed a simple sensitivity analysis using hourly rain gauge data from the Turkey River basin (see Fig. 1) for the entire period of 1 May–15 June 2013. We applied VIL_{avg} of 3.0, 4.0, 4.5, and 5.0 and generated hourly radar rainfall estimates for all different VIL_{avg} values. We then evaluated radar estimates using rain gauge data, and the results showed that VIL_{avg} of 3.0 and 4.0 performed slightly better than others. The performance difference between 3.0 and 4.0 seemed negligible and did not show a distinguishable difference. Therefore, we selected 4.0 as the region-growing parameter to reduce the potential chance of containing the BB effect in convective areas, rather than taking slightly larger convective zones as shown in Fig. 5.

3.3. Detection of wind turbine clutter

VIL describes vertical development of precipitation systems and implies the degree of convective activities for specific locations. Given the features of radar returns from wind turbines (e.g., Hood et al. 2010; Seo et al. 2015b), their VIL should be significantly smaller than that for an actual convective cell, despite their comparable reflectivity strength observed. This is mainly caused by their weak vertical extension (limited tower height and blade size) and sudden decrease of reflectivity at higher tilts. The reflectivity values obtained from the wind turbine returns are often > 50 dBZ, even at a range over 100 km from the radar, and these returns occasionally appear together with rain echoes. Fig. 6 shows three example cases of clustered wind turbine clutter: (a) widespread clutter contamination in a clear (no rain) mode; (b) mixed returns from ground and some wind farm locations in a rain mode; and (c) wind farm clutter embedded in rain echoes. We present the maps of base scan reflectivity and our VIL estimation for each case in Fig. 6. Insets in Fig. 6 show detailed reflectivity and the VIL patterns of each region marked by small red boxes in the reflectivity maps. While the clutter at far ranges shown in the insets of Fig. 6(a) and (c) yields significant VIL contributed by the wide vertical beam width at those ranges, the estimated VIL for those near the radar shown in the inset of Fig. 6(b) does not seem significant. The cases in Fig. 6(a) and (c) imply that the convective cells defined by the proposed method in section 3.2 need to pass an additional check (e.g., vertical continuity) to filter out these clutter cases.

To develop a clutter detection strategy, we further examined the VIL distributions of radar returns from both wind turbines and precipitation systems conditioning on the reflectivity strength. We analyzed the cases shown in Figs. 5(a) and 6(a) using two reflectivity ranges (> 50 and > 25 dBZ) and presented their VIL distributions in Fig. 7. As illustrated in Fig. 6(a), there are a variety of clutter returns in terms of the reflectivity strength, and the two ranges represent very intense (> 50 dBZ) and relatively mild (> 25 dBZ) interference by the clusters of wind turbines, respectively. For the intense reflectivity range, we can observe that most clutter cells (about 80%) exist within a low range of VIL (e.g., 0.0–2.0 kg/m^2), and rain cells make little contribution within this range. On the other hand, the mild reflectivity range in Fig. 7(a) shows that about 20% of rain cells are below the VIL value of 1.0, and this also indicates the requirement for additional procedures to exclude rain cells. The shaded areas in Fig. 7 specify the proposed conditional VIL thresholds (VIL < 1.0 for Z > 25 dBZ; and VIL < 2.0 for Z > 50 dBZ) to identify wind turbine clutter cells. We perform a vertical continuity check as an additional procedure to exclude rain cells, particularly for the ones included in the clear rain case shown in Fig. 7(a). This continuity check inspects the vertical gradient of reflectivity between successive tilts using the lowest three tilts (e.g., typically 0.5°, 1.0°, and 1.5° elevation angles in a rain mode) and restores rain cells when there is no distinguishable reflectivity drop at higher tilts. For example, the procedure regards cases as wind farm echoes when there is no echo (e.g., < 10 dBZ) observed at higher tilts (although we observed some significant echo at the lowest tilt), or reflectivity difference between successive tilts are > 20 dBZ. We then use the detected cells as seeds to expand the clutter regions with the parameters of reflectivity values, 15 and 40 dBZ for no rain and rain regions, respectively. We present our detection results together with precipitation type classification in Fig. 8 for the presented cases in Fig. 7. All cases in Fig. 8 demonstrate successful clutter detection in both clear and rainy cases. However, we also note that our proposed approach was partially unsuccessful in detecting few cases of mild and strong clutter observed in Fig. 8(a). Our data quality control (e.g., Seo et al. 2015b) can readily handle this handful of turbine echoes, as well as the ground clutter shown in Fig. 8. We did not apply the quality control procedure in Fig. 8 to show all the turbine clutter detected. We also examined many other rain cases to make sure our detection approach does not erroneously remove rain echoes.

4. Evaluation

In this section, we quantitatively assess the rainfall estimation improvement accomplished using the proposed classification method. To enable this assessment, we applied different reflectivity-rain rate (Z-R) relationships according to the classified types (i.e., $Z = 300R^{1.4}$ for convective; and $Z = 200R^{1.6}$ for stratiform) and compared the results with those from the case without classification. We uniformly applied one of the estimators (e.g., $Z = 300R^{1.4}$) for the case without classification. This uniform estimator had been applied to the U.S. official QPE algorithm of WSR-88Ds for many years (Fulton et al. 1998), and is also currently used as the main element to generate the real-time IFC rainfall estimates (e.g., Krajewski et al. 2017).

We evaluate two rainfall products, those of which were processed with/without precipitation classification, using hourly rain gauge data over the Turkey River basin (see Fig. 1) for the six-week period of 1 May–15 June 2013. Fig. 9 shows six-week rainfall accumulation maps, centered on the KARX radar, with/without precipitation classification. The maps shown in Fig. 9 (e.g., the regions marked by the dashed circles) demonstrate that classification tends to increase rainfall amounts in the relatively light rain regions. This period was quite wet and offers enough rain events to allow us to examine the different event features and the event-dependent (e.g., convective/stratiform or heavy/light) performance in rainfall estimation. Based on rain gauge records and visual inspection of the IFC rain rate maps archived for the period, we selected 16 rain events with various durations and rainfall intensities. Table 1 lists each individual event period, duration, and maximum rainfall intensity (mm/h) observed during the event. The maximum intensity in Table 1 implies an event feature because a rain event with high maximum intensity is likely a convective one, for which differences between two estimation procedures (with/without classification) tend to be minimized.

Fig. 10 shows our rain gauge evaluation results for all 16 rain events; the performance of the two procedures is measured by multiplicative bias (B), correlation (r), mean absolute error (MAE), and root mean square error (RMSE). These metrics were calculated using hourly radar-gauge pairs obtained for all 20 gauge locations. The values of all metrics are also presented in Table 2. The multiplicative bias is represented as a ratio between radar estimates (R) and rain gauge observations (G). In Fig. 10, the bias seems highly variable among the selected events, although the correlation is quite consistent (e.g., > 0.7)

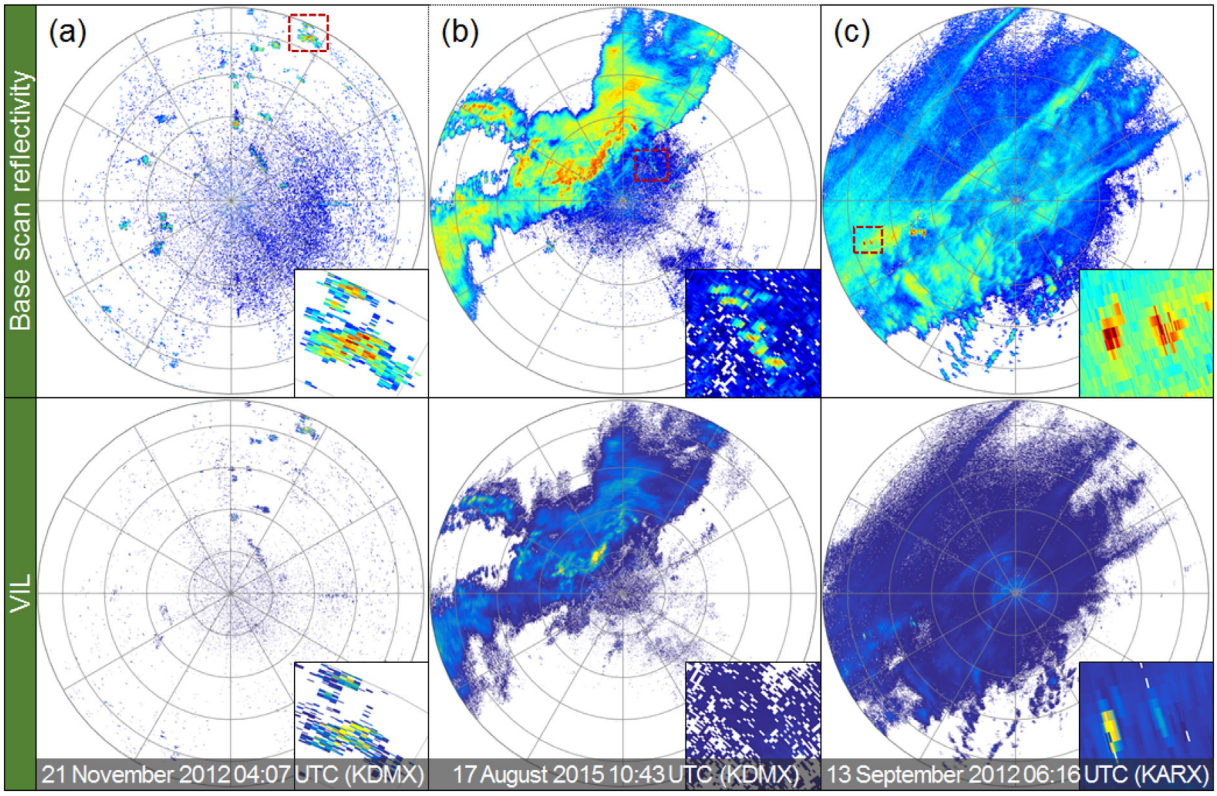

Fig. 6. Maps of base scan reflectivity and VIL for three example cases of clustered wind turbine clutter: (a) widespread clutter in a clear mode; (b) wind turbine clutter mixed with ground clutter in a rain mode; and (c) embedded wind turbine clutter within precipitation echoes. The insets show detailed spatial patterns for the regions as indicated by the red dashed squares. Colour scales are identical to the ones in Figs. 2 and 4. (For interpretation of the references to colour in this figure legend, the reader is referred to the web version of this article.)

for most events. We notice that some light rain events (6, 13, and 16) led to significant overestimations (over 150%), indicated by their bias values. For these light rain cases, the multiplicative bias is sensitive to a low range of rainfall magnitude, and we confirmed that the significant data portion of all three events belongs to a rainfall range below 1.0 mm/h. It is also recognized that QPE for such rainfall regime is quite challenging, including with polarimetric estimation approaches (e.g., Ryzhkov et al. 2005; Cifelli et al. 2011). Overall, the performance illustrated in Fig. 10 does not show prominent differences between the two estimation procedures for most event cases, whereas event 7 shows a considerable error reduction in MAE and RMSE. For most cases in Fig. 10, a reflectivity range for stratiform rain (e.g., 0–30 dBZ) does not tend to yield significant rainfall differences based on the application of the two different *Z-R*s used in this study. We note that one factor that can make notable differences is the BB effect, as seen in the clear performance difference observed in the event 7. We ensured the presence of the melting layer and its effect on the reflectivity observations over the basin area during the entire period of event 7. We also applied a VPR correction scheme as documented in Seo et al. (2011); we present the correction results in Fig. 11. The improvement in the current VPR correction compared to the one in Seo et al. (2011) is that the current scheme corrects (adjusts) reflectivity values within regions identified as stratiform precipitation only. Fig. 11 shows that our correction reduces the overestimation tendency caused by the BB effect, and the estimated rainfall values with VPR correction in Fig. 11 seem much closer to the one-to-one line. This verifies the success of our VIL estimation and subsequent classification for the regions affected by the BB effect.

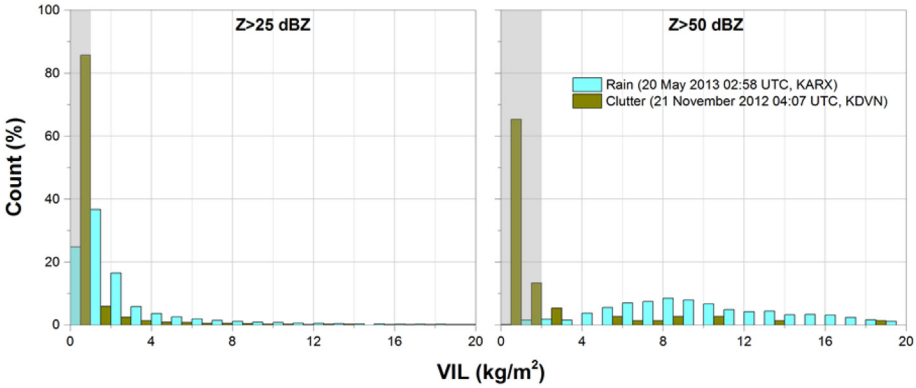

Fig. 7. VIL distributions (histograms) conditioned on reflectivity strength ($>$ 25 and $>$ 50 dBZ) for the rain and widespread wind turbine cases shown in Figs. 5(a) and 6(a), respectively. The gray colored areas indicate our threshold selection depending on the reflectivity strength.

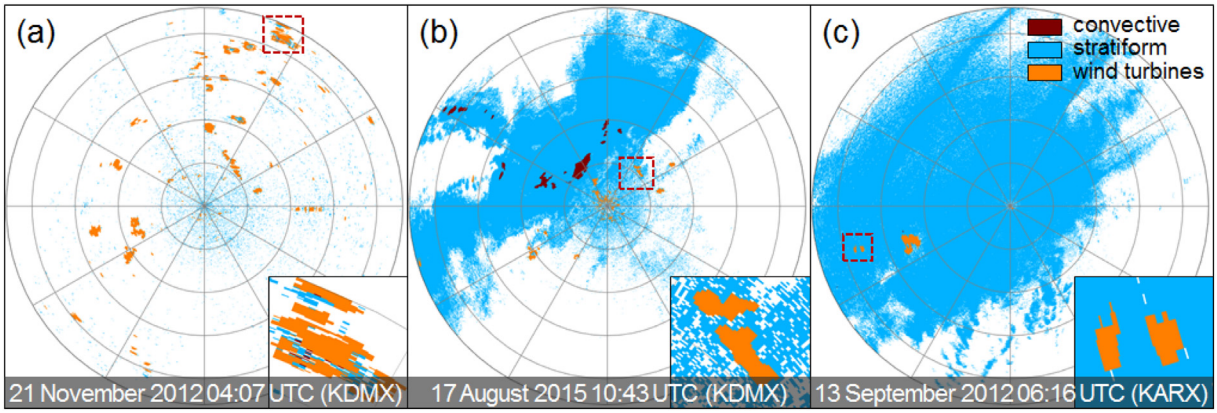

Fig. 8. Classification maps including the detection of wind turbine clutter for the three cases presented in Fig. 6. The insets show the detailed spatial patterns of the clutter identification for the red dashed regions. (For interpretation of the references to colour in this figure legend, the reader is referred to the web version of this article.)

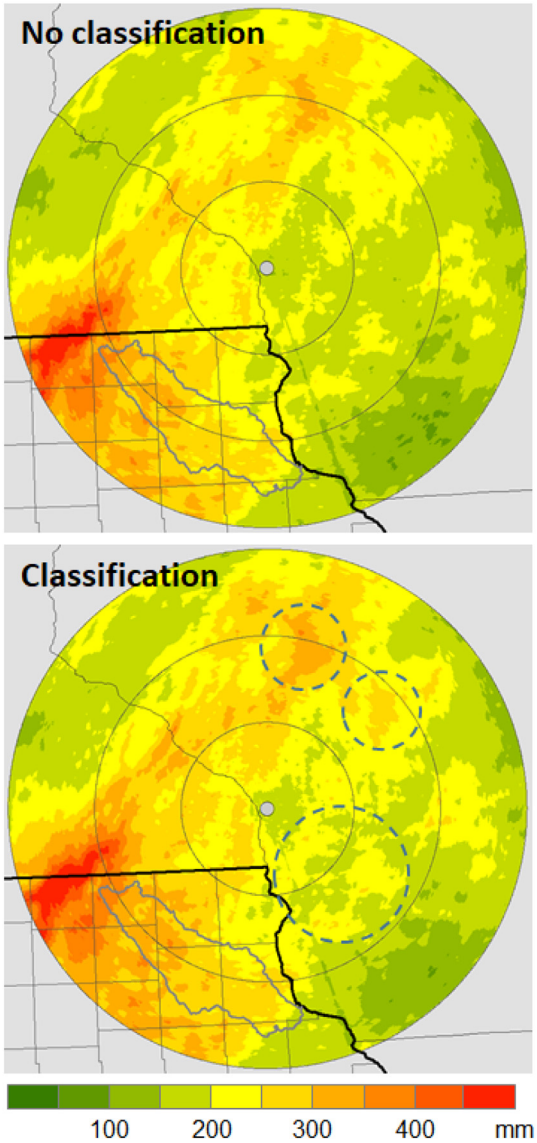

Fig. 9. Rainfall accumulation maps with/without classification for the six-week period of 1 May–15 June 2013. The dashed circles in "Classification" indicate major differences between the two accumulation maps. The maximum range shown in the map is 150 km, and the circular lines centered on the KARX radar demarcate every 50 km distance from the radar.

Table 1
List of selected rain events for the entire period of 1 May–15 June 2013.

Event	Event period (UTC)	Duration (h)	Maximum intensity (mm/h)
1	2 MAY 08:00–4 May 11:00	51	8.6
2	8 May 22:00–10 May 04:00	30	20.1
3	19 May 10:00–20 May 09:00	23	29.5
4	21 May 01:00–07:00	6	21.6
5	22 May 20:00–23 May 08:00	12	9.3
6	25 May 03:00–20:00	17	3.1
7	26 May 12:00–19:00	7	14.6
8	28 May 0900–12:00	3	4.6
9	29 May 20:00–30 May 06:00	10	44.1
10	30 May 22:00–31 May 00:00	2	19.2
11	4 June 12:00–5 June 05:00	17	12.2
12	5 June 08:00–6 June 02:00	18	5.5
13	8 June 21:00–10 June 02:00	29	3.1
14	12 June 10:00–13:00	3	37.2
15	12 June 21:00–13 June 03:00	6	29.3
16	15 June 06:00–15 June 13:00	7	3.9

5. Summary and discussion

We demonstrated the utility of the VIL application to the classification of precipitation types (convective/stratiform) and the detection of wind turbine effects present in radar echoes. A number of studies have investigated the two subjects separately, but herein we propose to examine these subjects together because both are likely well characterized by the vertical signatures observed from radar data. This new approach proposed for VIL estimation uses three-dimensional radar reflectivity data and temperature sounding retrieved from a numerical model (e.g., Rapid Refresh) analysis. Our approach detects reflectivity enhancement within the melting layer identified based on temperature sounding, adjusts the enhancement using the local VPR, and reduces probable VIL overestimation caused by the BB effects. We tested the proposed VIL estimation for many cases observed in Iowa and demonstrated its usefulness using the two representative BB cases, as shown in Fig. 4.

Unlike other studies that involve a complex decision tree (e.g., Steiner et al. 1995; Qi et al. 2013), the classification procedure described in this study is quite simple and includes two decision factors: (1) a VIL threshold (6.5 kg/m^2) to define convective cores; and (2) a region-growing parameter (4.0 kg/m^2 of VIL) to expand convective regions. We apply these two factors consistently over the entire radar domain without any range (or altitude) limitation, while other aforementioned studies require a set of different reflectivity thresholds depending on temperature, range, and altitude. We also avoid using

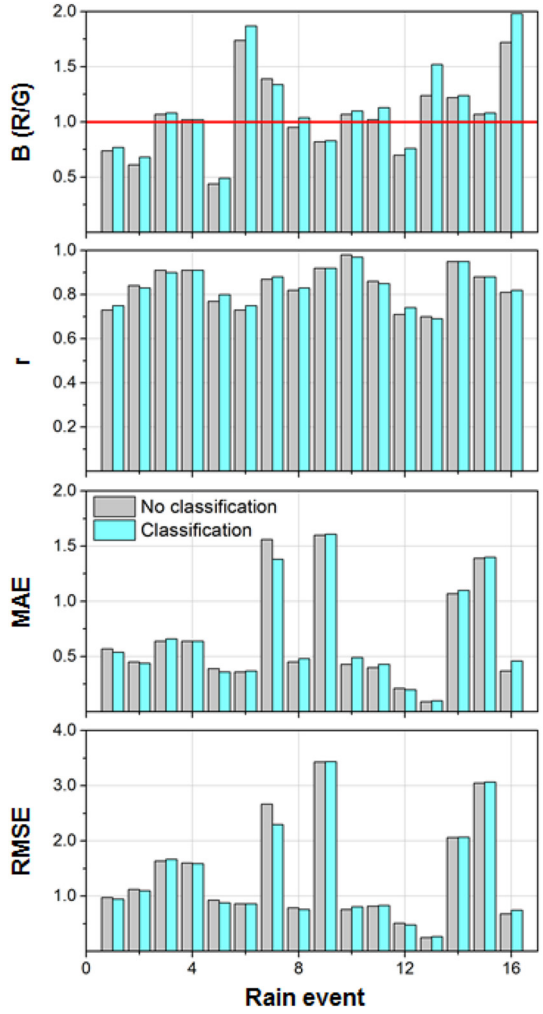

Fig. 10. Rain gauge evaluation results for rainfall estimates with/without precipitation classification using 16 rain events selected from the period of 1 May–15 June 2013. The performance (accuracy) is measured by multiplicative bias (B), correlation (r), mean absolute error (MAE), and root mean square error (RMSE).

Table 2
Rain gauge evaluation results quantified by the statistical metrics for the listed rain events in Table 1.

Event	No classification				Classification				Maximum intensity (mm/h)
	B	r	MAE (mm)	RMSE (mm)	B	r	MAE (mm)	RMSE (mm)	
1	0.74	0.73	0.57	0.98	0.77	0.75	0.54	0.95	8.6
2	0.61	0.84	0.45	1.12	0.68	0.83	0.44	1.10	20.1
3	1.07	0.91	0.64	1.64	1.08	0.90	0.66	1.67	29.5
4	1.02	0.91	0.64	1.60	1.02	0.91	0.64	1.59	21.6
5	0.44	0.77	0.39	0.93	0.49	0.80	0.36	0.88	9.3
6	1.74	0.73	0.36	0.86	1.87	0.75	0.37	0.86	3.1
7	1.39	0.87	1.56	2.67	1.34	0.88	1.38	2.30	14.6
8	0.95	0.82	0.45	0.79	1.04	0.83	0.48	0.76	4.6
9	0.82	0.92	1.60	3.43	0.83	0.92	1.61	3.44	44.1
10	1.07	0.98	0.43	0.76	1.10	0.97	0.49	0.81	19.2
11	1.02	0.86	0.40	0.82	1.13	0.85	0.43	0.83	12.2
12	0.70	0.71	0.21	0.51	0.76	0.74	0.20	0.48	5.5
13	1.24	0.70	0.09	0.25	1.52	0.69	0.10	0.27	3.1
14	1.22	0.95	1.07	2.06	1.24	0.95	1.10	2.07	37.2
15	1.07	0.88	1.39	3.05	1.08	0.88	1.40	3.07	29.3
16	1.72	0.81	0.37	0.68	1.98	0.82	0.46	0.75	3.9

reflectivity in the (convective) region-growing procedure because it is vulnerable to the BB effects. Instead, we adhere to VIL, for which the BB effects are already mitigated, and selected a parameter value of 4.0 (an average of neighboring pixels) based on a visual inspection and simple sensitivity analysis. The sensitivity analysis tested several VIL values by performing a radar-gauge comparison.

We evaluated the proposed precipitation classification method using data from a high-quality, high-density rain gauge network deployed in the Turkey River basin, Iowa. The evaluation metrics (e.g., bias) show that the estimation performance seems highly variable among the presented event cases (Fig. 10). We speculate that the bias fluctuation observed in Fig. 10 is likely not associated with the proposed classification method, but rather accounts for the limitation of the *R(Z)* estimators for some event cases. We have been making an effort to implement and test the most recent polarimetric estimator (e.g., specific attenuation) documented in Ryzhkov et al. (2014) and Wang et al. (2019), which may resolve the issue of estimation variability on different event characteristics (e.g., drop size distribution). The rainfall accumulation maps shown in Fig. 12 illustrate an early result on the application of specific attenuation in conjunction with the proposed quality control method in this study. Based on a visual inspection, we verify that the proposed VIL method effectively removes significant wind farm echoes observed in the map of Multi-Radar Multi-Sensor (MRMS, Zhang et al. 2016). Because a quantitative evaluation (e.g., accuracy) of our new estimation presented in Fig. 12 is not within the scope of this study, we hope to report the result of this effort in the near future. The proposed classification method shows improved performance (compared to no classification) primarily for non-convective cases in Fig. 10. The convective cases (e.g., events 3, 9, and 14) show similar performance because the effect of classified stratiform area within the limited coverage of the rain gauge network is minimized in those cases. We also demonstrated the usefulness of our precipitation classification for a VPR correction procedure over the regions affected by the BB effects. The VPR correction without proper classification of precipitation types might lead to significant overestimation over convective regions placed at far ranges (e.g., Bellon et al. 2005).

The detection of wind turbine clutter is challenging because of their rain-like patterns in radar returns (e.g., Seo et al. 2015b). We note that some earlier classification studies may misclassify wind turbine clutter as convective cores if preprocessing (e.g., data quality control) fails to remove them. For example, Qi et al. (2013) suggested a reflectivity threshold of 45 dBZ below the freezing level within a 25 km radar range. However, we have observed many cases of wind turbine clutter where reflectivity values were even higher than 50 dBZ over a variety of radar ranges in sufficiently warm environments. Since wind turbines are typically clustered to optimize their operational efficiency (which makes the clutter feature similar to isolated precipitation), it is hard to remove the non-precipitation returns based on application of a simple threshold of polarimetric observations (e.g., copolar correlation coefficient or variability of differential phase). As such, we developed a new idea that can detect wind turbine clutter based on the estimated VIL because it is unlikely that the effect of wind turbines is extended vertically compared to actual convective cells, which show comparable reflectivity strength. The cases shown in Fig. 8 verify our proposed idea and its applicability to various wind turbine effects (e.g., clutter embedded in rain echoes). However, we note that there is a trade-off between removing clutter and preserving rain echoes, and application of a strong filter may lead to the removal of some portion of light rain.

Acknowledgments

This study was supported by the Iowa Flood Center. The second author was partially supported by the Rose & Joseph Summers endowment.

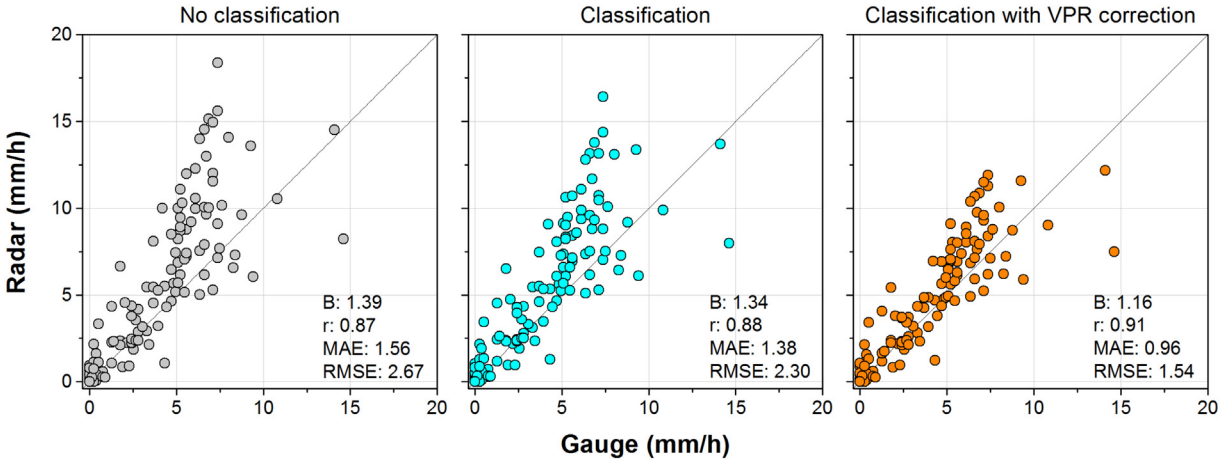

Fig. 11. A scatter plot of radar-gauge comparisons for the event 7 in Table 1. Given the evaluation metrics, the VPR correction shows significant improvement, i.e. reduction of rainfall overestimation, arising from the BB effect.

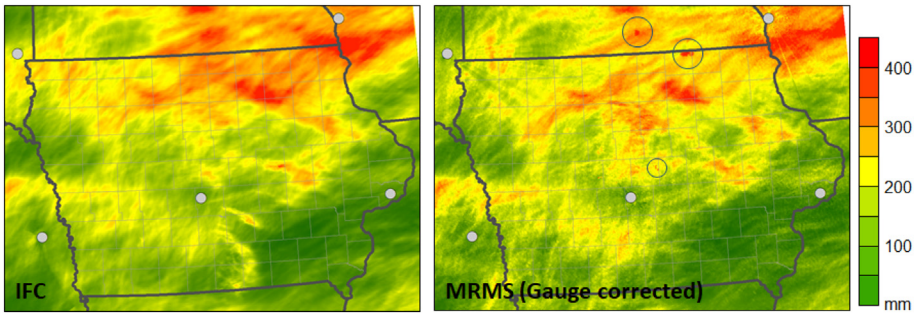

Fig. 12. IFC (using specific attenuation with the proposed VIL method) and MRMS Rainfall accumulation maps for September 2016. The circles shown in the MRMS map indicate wind farm locations.

Declaration of interests

The authors declare that they have no known competing financial interests or personal relationships that could have appeared to influence the work reported in this paper.

References

Adams, R., Bischof, L., 1994. Seeded region growing. IEEE T. Pattern Anal. 16, 641–647.
Anagnostou, E., 2004. A convective/stratiform precipitation classification algorithm for volume scanning weather radar observations. Meteorol. Appl. 11, 291–300.
Austin, P.M., Bemis, A.C., 1950. A quantitative study of the "BB" in radar precipitation echoes. J. Appl. Meteorol. 7, 145–151.
Bellon, A., Lee, G., Zawadzki, I., 2005. Error statistics of VPR corrections in stratiform precipitation. J. Appl. Meteorol. 44, 998–1015.
Benjamin, S.G., Weygandt, S.S., Brown, J.M., Hu, M., Alexander, C.R., Smirnova, T.G., Olson, J.B., James, E.P., Dowell, D.C., Grell, G.A., Lin, H., Peckham, S.E., Smith, T.L., Moninger, W.R., Kenyon, J.S., Manikin, G.S., 2016. A north American hourly assimilation and model forecast cycle: the Rapid Refresh. Mon. Wea. Rev. 144, 1669–1694.
Boudevillain, B., Andrieu, H., 2003. Assessment of vertically integrated liquid (VIL) water content radar measurement. J. Atmos. Ocean. Technol. 20, 807–819.
Brown, R.A., Wood, V.T., Steadham, R.M., Lee, R.R., Flickinger, B.A., Sirmans, D., 2005. New WSR-88D volume coverage pattern 12: results of field tests. Weather Forecast. 20, 385–393.
Caracciolo, C., Porcù, F., Prodi, F., 2008. Precipitation classification at mid-latitudes in terms of drop size distribution parameters. Adv. Geosci. 16, 11–17.
Chapon, B., Delrieu, G., Gosset, M., Boudevillain, B., 2008. Variability of rain drop size distribution and its effect on the *Z–R* relationship: a case study for intense Mediterranean rainfall. Atmos. Res. 87, 52–65.
Cifelli, R., Chandrasekar, V., Lim, S., Kennedy, P.C., Wang, Y., Rutledge, S.A., 2011. A new dual-polarization radar rainfall algorithm: Application in Colorado precipitation events. J. Atmos. Ocean. Technol. 28, 352–364.
Creutin, J.D., Andrieu, H., Faure, D., 1997. Use of a weather radar for the hydrology of a mountainous area. Part II: radar measurement validation. J. Hydrol. 193, 26–44.
Crum, T., Alberty, R., 1993. The WSR-88D and the WSR-88D operational support facility. Bull. Am. Meteorol. Soc. 74, 1669–1687.
Crum, T.D., Alberty, R.L., Burgess, D.W., 1993. Recording, archiving, and usingWSR-88D data. Bull. Am. Meteorol. Soc. 74, 645–653.
French, M.N., Andrieu, H., Krajewski, W.F., 1995. Uncertainty in vertically integrated liquid water content due to radar reflectivity observation error. J. Atmos. Ocean. Technol. 12, 404–409.
Greene, D.R., Clark, R.A., 1972. Vertically Integrated Liquid water–a new analysis tool. Mon. Wea. Rev. (7), 548–552.
Hood, K., Torres, S., Palmer, R., 2010. Automatic detection of wind turbine clutter for weather radars. J. Atmos. Ocean. Technol. 27, 1868–1880.
Johnson, J.T., MacKeen, P.L., Witt, A., Mitchell, E.D., Stumpf, G.J., Eilts, M.D., Thomas, K.W., 1998. The storm cell identification and tracking algorithm: an enhanced WSR-88D algorithm. Weather Forecast. 13, 263–276.
Krajewski, W.F., Ceynar, D., Demir, I., Goska, R., Kruger, A., Langel, C., Mantilla, R., Niemeier, J., Quintero, F., Seo, B.-C., Small, S., Weber, L., Young, N., 2017. Real-time flood forecasting and information system for the State of Iowa. Bull. Am. Meteorol. Soc. 98, 539–554.
Kusiak, A., Song, Z., 2010. Design of wind farm layout for maximum wind energy capture. Renew. Energy 35, 685–694.
Li, N., Tang, G., Zhao, P., Hong, Y., Gou, Y., Yang, K., 2017. Statistical assessment and hydrological utility of the latest multi-satellite precipitation analysis IMERG in Ganjiang River basin. Atmos. Res. 183, 212–223.
Llasat, M.C., Ceperuelo, M., Rigo, T., 2007. Rainfall regionalization on the basis of the precipitation convective features using a raingauge network and weather radar observations. Atmos. Res. 83, 415–426.
Löhnert, U., Crewell, S., Simmer, C., 2004. An integrated approach toward retrieving physically consistent profiles of temperatures, humidity, and cloud liquid water. J. Appl. Meteorol. 43, 1295–1307.
Marshall, J.S., Palmer, W.M.K., 1948. The distribution of raindrops with size. J. Appl. Meteorol. 5, 165–166.
Matrosov, S.Y., 2009. A method to estimate vertically integrated amounts of cloud ice and liquid and mean rain rate in stratiform precipitation from radar and auxiliary data. J. Appl. Meteorol. Clim. 48, 1398–1410.
Mesinger, F., DiMego, G., Kalnay, E., Mitchell, K., Shafran, P.C., Ebisuzaki, W., Jovic, D., Woollen, J., Rogers, E., Berbery, E.H., Ek, M.B., Fan, Y., Grumbine, R., Higgins, W., Li, H., Lin, Y., Manikin, G., Parrish, D., Shi, W., 2006. North American regional reanalysis. Bull. Am. Meteorol. Soc. 87, 343–360.
Qi, Y., Zhang, J., Zhang, P., 2013. A real-time automated convective and stratiform precipitation segregation algorithm in native radar coordinates. Q. J. R. Meteorol. Soc. 139, 2233–2240.
Quintero, F., Krajewski, W.F., Mantilla, R., Small, S., Seo, B.-C., 2016. A spatial–dynamical framework for evaluation of satellite rainfall products for flood prediction. J.

Hydrometeorol. 17, 2137–2154.
Ryzhkov, A., Schuur, T., Burgess, D.W., Heinselman, P.L., Giangrande, S.E., Zrnic, D.S., 2005. The joint polarization experiment: polarimetric rainfall measurements and hydrometeor classification. Bull. Am. Meteorol. Soc. 86, 809–824.
Ryzhkov, A., Diederich, M., Zhang, P., Simmer, C., 2014. Potential utilization of specific attenuation for rainfall estimation, mitigation of partial beam blockage, and radar networking. J. Atmos. Ocean. Technol. 31, 599–619.
Auer, Jr., A.H., Sand, W., 1966. Updraft measurements beneath the base of cumulus and cumulonimbus clouds. J. Appl. Meteorol. 5, 461–466.
Seo, D.J., Briedenbach, J.P., Johnson, E.R., 1999. Real-time estimation of mean field bias in radar rainfall data. J. Hydrol. 223, 131–147.
Seo, B.-C., Krajewski, W.F., Kruger, A., Domaszczynski, P., Smith, J.A., Steiner, M., 2011. Radar-rainfall estimation algorithms of Hydro-NEXRAD. J. Hydroinf. 13, 277–291.
Seo, B.-C., Dolan, B., Krajewski, W.F., Rutledge, S., Petersen, W., 2015a. Comparison of single and dual polarization based rainfall estimates using NEXRAD data for the NASA Iowa Flood Studies Project. J. Hydrometeorol. 16, 1658–1675.
Seo, B.-C., Krajewski, W.F., Mishra, K.V., 2015b. Using the new dual-polarimetric capability of WSR-88D to eliminate anomalous propagation and wind turbine effects in radar-rainfall. Atmos. Res. 153, 296–309.
Seo, B.-C., Krajewski, W.F., Quintero, F., ElSaadani, M., Goska, R., Cunha, L.K., Dolan, B., Wolff, D.B., Smith, J.A., Rutledge, S.A., Petersen, W.A., 2018. Comprehensive evaluation of the IFloodS radar-rainfall products for hydrologic applications. J. Hydrometeorol. 19, 1793–1813.
Skripniková, K., Řezáčová, D., 2014. Radar-based hail detection. Atmos. Res. 144, 175–185.
Steiner, M., Houze Jr., R.A., Yuter, S.E., 1995. Climatological characterization of three-dimensional storm structure from operational radar and rain gauge data. J. Appl. Meteorol. 34, 1978–2007.
Stewart, R.E., Marwitz, J.D., Pace, J.C., Carbone, R.E., 1984. Characteristics through the melting layers of stratiform clouds. J. Atmos. Sci. 41, 3227–3237.
Villarini, G., Krajewski, W.F., 2010. Review of the different sources of uncertainty in single polarization radar-based estimates of rainfall. Surv. Geophys. 31, 107–129.
Wang, Y., Cocks, S., Tang, L., Ryzhkov, A., Zhang, P., Zhang, J., Howard, K., 2019. A prototype quantitative precipitation estimation algorithm for operational S-band polarimetric radar utilizing specific attenuation and specific differential phase: Part I-Algorithm description. J. Hydrometeorol. 20, 985–997.
Witt, A., Eilts, M.D., Stumpf, G.J., Johnson, J.T., Mitchell, E.D., Thomas, K.W., 1998. An enhanced hail detection algorithm for the WSR-88D. Weather Forecast. 13, 286–303.
Zhang, J., Qi, Y., 2010. A real-time algorithm for the correction of brightband effects in radar-derived QPE. J. Hydrometeorol. 11, 1157–1171.
Zhang, J., Howard, K., Langston, C., Kaney, B., Qi, Y., Tang, L., Grams, H., Wang, Y., Cocks, S., Martinaitis, S., Arthur, A., Cooper, K., Brogden, J., Kitzmiller, D., 2016. Multi-Radar Multi-Sensor (MRMS) quantitative precipitation estimation: initial operating capabilities. Bull. Am. Meteorol. Soc. 97, 621–638.